STRUCTURAL AND TEXTURAL MODIFICATIONS OF ZrO$_2$ INDUCED BY La$_2$O$_3$ ADDITION, THERMAL TREATMENT AND REDUCING PROCESS

K. Aribi[1], M. Ghelamallah[1], A. Bellifa[1], P. Granger[2], A. Choukchou-Braham[3]

[1]*Laboratoire de Matériaux, Applications et Environnement, Université Mustapha Stambouli, Mascara, Algeria*
 E-mail: gh_madani@hotmail.com
[2]*Unité de Catalyse et de Chimie du Solide, Université Lille 1, Sciences et Technologies, Villeneuve d'Ascq Lille, France*
[3]*Laboratoire de Catalyse et Synthèse en Chimie Organique, Université Abou Bekr Belkaid, Tlemcen, Algeria*

Lanthana-doped zirconium oxide may strongly influence the solid state reaction. A series of samples denoted Zr$_x$La$_{1-x}$ (where x = atomic percentage of the element) are prepared by hydrolysis in the neutral medium from ZrO$_2$ and La$_2$O$_3$. These samples are calcined under air at 450, 900, and 1200 °C, then characterized by specific surface area (BET), X-ray diffraction (XRD), scanning electron microscopy (SEM) and thermoreductions programmed under H$_2$ (TPR—H$_2$). The results show that after calcination at 450 °C, the lanthanum addition increases slightly the zirconia surface area and the XRD analysis does not reveal any interaction between two oxides. After calcination at 900 °C, sintering appears and oxides lose half of their surface area. Lanthanum is not inserted into the structure of ZrO$_2$, while some interaction occurs between lanthanum and zirconium oxide. At 1200 °C, the sintering of the samples is very important; the specific surface is about 1 m^2/g; XRD results show that Zr$_x$La$_{1-x}$ are formed basically by three mixed oxides: La$_2$Zr$_2$O$_7$, La$_{0.5}$Zr$_{0.5}$O$_{1.75}$, La$_{0.46}$Zr$_{0.54}$O$_{1.77}$, which is confirmed by the SEM method. H$_2$-TPR experiments confirm that changes in the reducibility can reflect some alterations of the nature of interactions between ZrO$_2$ and La$_2$O$_3$. Preliminary experiments on zirconia do not reveal the occurrence of significant reduction processes. On the other hand, extensive reduction of La$_2$O$_3$ is much more accentuated for lanthana samples. At high temperatures, a significant lessening in the H$_2$ consumption suggests that ZrO$_2$ would likely interact with La$_2$O$_3$, which is confirmed in the results indicating the presence of the pyrochlore type of oxides mentioned above.

INTRODUCTION

Much attention is focused on zirconia (nanoparticles, ceramic, material, oxide, nanocrystalline) because of their large number of uses. Compounds have been actively studied owing to their enormous applications in electrochemical devices such as oxygen pumps, oxygen sensors, and solid state electrolytes in fuel cells [1—4]. Zirconia-based compounds are used in solid oxide fuel cells (SOFC). However, the low mechanical force and the high price becomes a barrier for the use of pure ZrO$_2$ [5]. The addition of elements such as REO, especially La$_2$O$_3$, can generally improve the physicochemical properties of ZrO$_2$ [6—9]. ZrO$_2$ is typically blended with lower-valence oxides such as Y$_2$O$_3$, TiO$_2$, SnO$_2$, and Al$_2$O$_3$ to form a solid solution [10—13].

Pyrochlore R$_2$Zr$_2$O$_7$ (R = rare-earth metal) compounds have been used as hosts for fluorescence centers and oxidation catalysts. Thus, a number of investigations have been conducted to evaluate the

electrical, optical, and catalytic properties of these materials [14, 15]. Particular attention has been given to pyrochlore $La_2Zr_2O_7$, which was found to form at cathode interfaces of SOFCs during high-temperature processing [16].

This phenomenon has been investigated as a means of synthesizing $La_2Zr_2O_7$ by a number of methods, including the solid-state reaction, nitric acid dissolution, and the sol-gel technique [17, 18]. However, the formation of pyrochlore $La_2Zr_2O_7$ has been achieved only by the sol-gel process [18]. Therefore, the ZrO_2—La_2O_3 system does not provide only the stabilization of high-temperature structures, it includes also pyrochloric-structured $La_2Zr_2O_7$ [17—20]. This means has the potential application as both catalyst [20] and thermal barrier [14], and it can also be synthesized by either solid-state reaction between oxides at 1500—1600 °C or the sol-gel process [17]. The physicochemical property of the La_2O_3—ZrO_2 system is studied with other synthesis methods. The properties, such as the cubic formation, annealing effects, are studied on nanocrystalline ZrO_2 with other synthesis methods [14, 15, 20, 21].

Because of benefits of the nanocrystalline La_2O_3—ZrO_2 system under study with the annealing temperature and dopant concentration, the objective of this work is the stabilization through the La_2O_3 addition, which may improve the zirconia-lanthanum textural and structural properties. The choice of La_2O_3 as a dopant is based on the mismatch between the ionic radii of ZrO_2 and La_2O_3, and the fact that their valences are nearly equal. The effect of varying the amount of the La_2O_3 addition on the phase equilibrium, microstructure, sintering, and grain growth of ZrLa is subsequently investigated.

EXPERIMENTAL

Sample preparation. ZrO_2 and La_2O_3 (99.9 % in mass) used in the current work were purchased from Merck. Their surface areas are about 21.2 and 5.3 m^2/g respectively. ZrO_2 was hydrolyzed in an excess of distilled, deionized (D.D) water at 80 °C for 16 h [22]. La_2O_3 was added to these solutions and the mixture was homogenized at the same temperature for 5 h, The products obtained were filtered and dried overnight in air at 120 °C. They are denoted as Zr_xLa_{1-x} (x = at.% of the element). This pre-treatment procedure yields original results based on the starting materials. Calcination was performed under the airflow of 3 l/h in a dynamic reactor with a heating rate of 10 deg./min and isothermal at 450, 900, and 1200 °C for 3 h.

Characterization. The BET surface area (S_{BET}) of the solids was measured from nitrogen physisorption at −196 °C using Micrometrics ASAP-2010. The sample was previously degassed under vacuum at 120 °C for 2 h, The volume of adsorbed N_2 was normalized to the standard temperature and pressure. The specific surface areas of the samples were calculated based on the BET method. The crystal phase and size of the samples were determined by X-ray diffraction (XRD) patterns using a Philips PW1800 diffractometer operated at 40 kV, 30 mA, using CuK_α radiation $K_{\alpha 1}$ (1.54056 Å), and $K_{\alpha 2}$ (1.54439 Å), the intensity ratio being about 0.5. The phase identification was performed using the Joint Committee on Powder Diffraction Standards (JCPDS) database. The crystal size of the samples was calculated from the half-width of the peak with the highest intensity of the crystal phase measured by XRD after the correction of the peak width for the instrumental broadening contribution, using the Debye-Scherrer equation : $D_{hkl} = 0.89\lambda/B_{hkl}\cos\theta$ [23].

H_2-Temperature-Programmed Reduction (H_2-TPR) experiments were carried out in a fixed-bed reactor. 50 mg of the sample were exposed to 5 vol.% H_2/Ar with a continuous flow rate of 50 ml/min. A linear increase in the reactor temperature was monitored from room temperature to 900 °C with a heating rate of 10 °C/min. The outlet hydrogen concentration was measured using an on-line gas chromatograph equipped with a thermal conductivity detector.

The scanning electron microscopy (SEM) analysis was performed on a Hitachi S-3400N apparatus operating at 7 kV with magnification values in the range 5000—15000. This instrument is equipped with an energy dispersive EDAX 9100 X-ray microanalyzer, which permitted analytical electron microscopy measurements. The samples were sputter-coated with gold.

Reducibility and textural properties of Zr_xLa_{1-x} *samples calcined at* 450, 900, *and* 1200 °C

Sample	Specific surface area, m²/g			S_{th}/S_{BET} [a]		H_2 uptake, μ/mol·g [b]	
	450 °C	900 °C	1200 °C	450 °C	900 °C	450 °C	900 °C
Zr_1La_0	25.0	17.5	< 1	3.8	4.2	34	89
$Zr_{0.95}La_{0.05}$	26.4	11.5	—	—	—	—	—
$Zr_{0.85}La_{0.15}$	25.0	11.1	—	0.6	2.2	1253	135
$Zr_{0.7}La_{0.3}$	27.5	—	1.3	0.6	—	1073	—
$Zr_{0.5}La_{0.5}$	16.1	—	1.3	—	—	—	—
Zr_0La_1	11.2	3.4	< 1	2.5	7.4	437	95

[a] S_{th} specific surface area calculated from $S_{th} = 6/\rho \cdot D_p$ assuming the cubic crystallite size D_p.
[b] On calcined samples from H_2—TPR experiments.

RESULTS AND DISCUSSION

Textural properties. The surface characterizations of the samples are summarized in Table 1. Averaged values underline higher values of the samples calcined at 450 °C. At this temperature, La_2O_3 was added to ZrO_2 mainly for $Zr_{0.85}La_{0.15}$, except for $Zr_{0.5}La_{0.5}$ where a decrease in the specific surface area is more accentuated. This decrease can be explained by the algebraic sum of surfaces of Zr_1La_0 (25.0 m²/g) and Zr_0La_1 (5.2 m²/g) samples: $S = 0.5 \cdot S_{Zr1La0} \cdot 0.5 \cdot S_{Zr0La1}$. The departure of physisorbed water molecules could be the reason for a weak increase in the surface for both $Zr_{0.7}La_{0.3}$ and $Zr_{0.95}La_{0.05}$ samples. This increase could appear due to enhanced fine homogenized by electrical forces between extra granular zirconium oxide and lanthanum oxide [24].

Regarding changes in the specific surface area after calcination at 900 °C, only a slight decrease is distinguishable. The decrease in the specific surface area is more accentuated for the Zr_0La_1 sample. Both $Zr_{0.95}La_{0.5}$ and $Zr_{0.85}La_{0.15}$ show practically the same specific surface area. This seems to be consistent with a loss of the specific surface area because of thermal sintering after exposure to 900 °C [25]. However, it seems obvious that it is more accentuated at 1200 °C. The specific surface area does not exceed 1 m²/g for both Zr_1La_0 and Zr_0La_1. The specific surfaces areas of $Zr_{0.7}La_{0.3}$ and $Zr_{0.5}La_{0.5}$ are in the same margin error.

A rough estimation of the theoretical specific surface area S_{th}, based on the crystallite sizes in Table 1 calculated from the X-ray line broadening, can be compared with the BET surface (S_{BET}) calculated from nitrogen physisorption. As seen, higher values of the ratio S_{th}/S_{BET} are mainly observed for Zr_0La_1 and Zr_1La_0, preliminary calcined in air at 900 °C, which suggests that a greater surface fraction is lost by densification of the crystallites compared to mixtures of the samples. This corresponds to a decrease in the free surface between elementary particles [26].

Structural properties. XRD patterns of Zr_xLa_{1-x} samples calcined at 450 °C are presented in Fig. 1. The reflections can be mainly attributed to the presence of bulk lanthanum oxide and hydroxide. The XRD patterns recorded from the $Zr_{0.85}La_{0.15}$ and $Zr_{0.7}La_{0.3}$ samples are dominated by the characteristic X-ray lines of zirconia. The XRD patterns of Zr_1La_0 calcined at 450 °C are reported in Fig. 1*a*. The analysis of these XRD patterns shows that calcination at 450 °C ensue the monoclinic phase to 2θ = 24.1 and 28.2°.

At 900 °C, the cubic phase appears at 2θ = 30.2 and 34.8° (Fig. 2*a*). In the literature we observe the characteristic peak of the tetragonal phase of pure ZrO_2 at 2θ = 30.2 and 34.8° and at 2θ = 35.2° [27], while the peaks of the ZrO_2 cubic phase are at 2θ = 30 and 34.8° [28]. Therefore, the diffraction peak at 2θ = 30 and 35° could be assigned to the tetragonal and/or cubic ZrO_2 phase. However, it
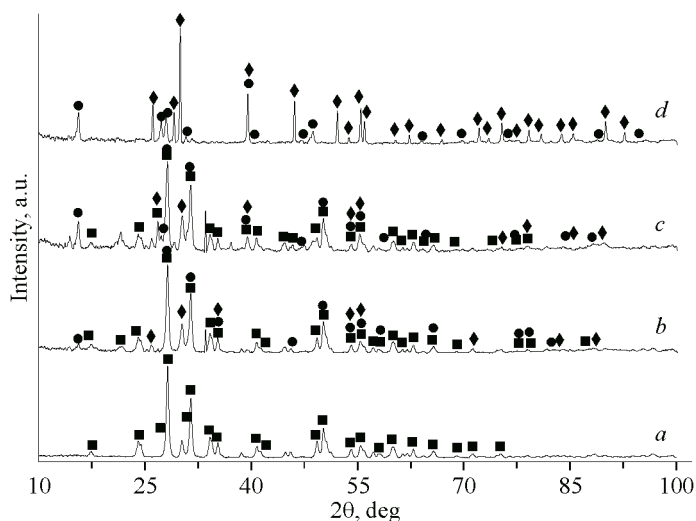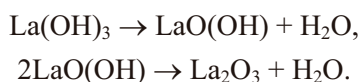
Fig. 1. XRD patterns recorded on the samples calcined in air at 450 °C: Zr_1La_0 (*a*), $Zr_{0.85}La_{0.15}$ (*b*), $Zr_{0.7}La_{0.3}$ (*c*), Zr_0La_1 (*d*); ZrO_2 (■), La_2O_3 (♦), $La(OH)_3$ (●)

is difficult to distinguish the tetragonal phase from the cubic one. The XRD patterns of Zr_0La_1 calcined under air at 900 °C show that the samples contain $La(OH)_3$, $LaO(OH)$, and La_2O_3, with the presence of reflections ascribed to bulk $LaO(OH)$ species on Zr_0La_1 (Fig. 2*c*).

The XRD patterns of Zr_xLa_{1-x} calcined under air at 900 °C (Fig. 2) show that there is no inter-action between zirconia and lanthanum oxide. The analysis of these spectra shows that these samples contain $La(OH)_3$ and $LaO(OH)$. The XRD patterns of $Zr_{0.85}La_{0.15}$ calcined under air at 900 °C ensure that the introduction of 15 % La_2O_3 mask the transformation monoclinic phase has the tetragonal and / or cubic phase. Lanthanum does not stabilize the tetragonal phase. Calcination at these two tempera-tures led to dehydrogenation of lanthanum trihydroxide, probably, by the following reaction:

$$La(OH)_3 \rightarrow LaO(OH) + H_2O,$$

$$2LaO(OH) \rightarrow La_2O_3 + H_2O.$$

At 1200 °C sintering induces an important transformation of the cubic phase to the monoclinic phase due to the internal rupture, which has been extensively reported in the literature [29].
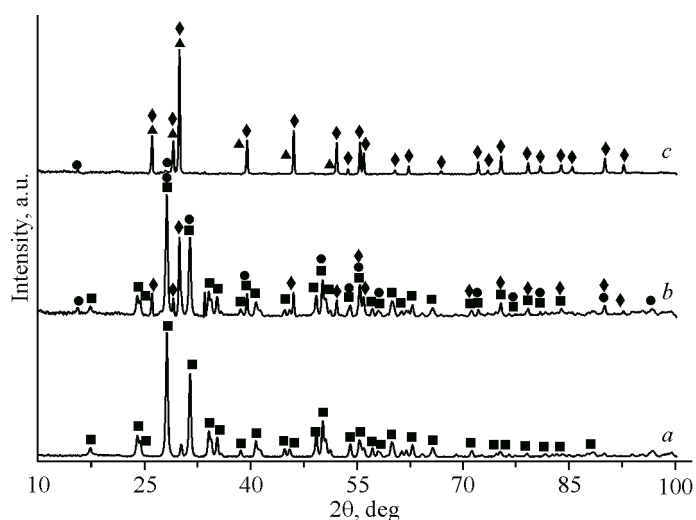

Fig. 2. XRD patterns recorded on the samples calcined in air at 900 °C: Zr_1La_0 (*a*), $Zr_{0.85}La_{0.15}$ (*b*), Zr_0La_1 (*c*); ZrO_2 (■), La_2O_3 (♦), $La(OH)_3$ (●), $LaO(OH)$ (▲)
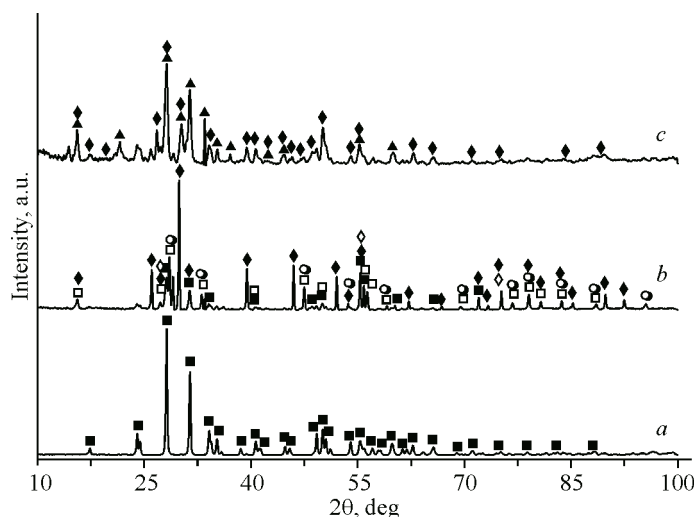
Fig. 3. XRD patterns recorded on the samples calcined in air at 1200 °C: Zr_1La_0 (*a*),
$Zr_{0.7}La_{0.3}$ (*b*), Zr_0La_1 (*c*); ZrO_2 (■), La_2O_3 (♦), LaO(OH) (▲), $La_2Zr_2O_7$ (□),
$La_{0.5}Zr_{0.5}O_{1.75}$ (○), $La_{0.46}Zr_{0.54}O_{1.77}$ (◊)
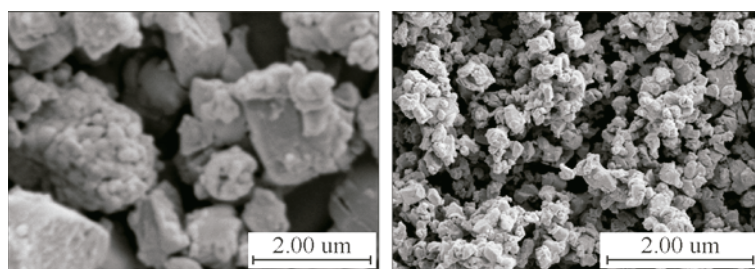

Fig. 4. SEM micrographs of the $Zr_{0.5}La_{0.5}$ samples calcined in air at 1200 °C

Additional X-ray lines ascribed to bulk lanthanum oxides and oxyhydroxides are observed for the samples calcined in air at 1200 °C. The increase in the calcination temperature to 1200 °C leads to the disappearance of the $La(OH)_3$ phase (Fig. 3).

The XRD patterns of $Zr_{0.7}La_{0.3}$ calcined at 1200 °C are represented in Fig. 3. The study of these spectra reveals an interaction between lanthanum and zirconium. Indeed, it forms a mixed phase $Zr_2La_2O_7$ and $Zr_{0.5}La_{0.5}O_{1.7}$ in the pyrochlore cubic form with spatial groups *Fd*-3*m*, ($a = 10.808$ Å) and *Fm*-3*m* ($a = 5.407$ Å) respectively. The particles formed are crystalline with an average size of about 30 nm. The results were confirmed by SEM (Fig. 4).

The crystallite size of hydroxides estimated from the XRD measurements using the usual Scherrer equation remained unchanged for the Zr_0La_1 samples after calcination at 900 °C, which indicates a good stability of this phase (Table 2). Some differences can be observed between the particle size determined by the surface area analysis and the particle measured by XRD, which characterizes the individual grains of a particle separated by grain boundaries.

The crystal size of ZrO_2—La_2O_3 oxides based on the XRD results (using the X-ray line broadening analysis) and the crystal phase of the oxides based on XRD were also presented in Table 1. The incorporation of the ZrO_2 into La_2O_3 could be a reason for a decrease in the crystal size of the oxides. The crystal size of ZrO_2—La_2O_3 slightly decreased with an increase in the La_2O_3 content. The incorporation of ZrO_2 into La_2O_3 could change the crystal phase from the monoclinic to pyrochlore cubic phase $Zr_2La_2O_7$.

Reducibility properties under H_2. The reducibility of calcined samples has been investigated by H_2—TPR experiments. As exemplified in Figs. 5 and 6, changes in the reducibility can reflect some

T a b l e 2

Structural properties of the Zr_xLa_{1-x} samples calcined at 450, 900, and 1200 °C
Average crystallite size (nm) *calculated from the characteristic reflections*
observed from XRD *patterns*

Sample	Temperature	ZrO_2	La_2O_3	LaO(OH)	$La(OH)_3$	$Zr_xLa_yO_z$
Zr_1La_0	450	10.81	—	—	—	—
	900	14.03	—	—	—	—
	1200	27.68	—	—	—	—
$Zr_{0.85}La_{0.15}$	450	69.64	84.29	—	70.19	—
	900	52.93	25.60	—	39.36	—
$Zr_{0.7}La_{0.3}$	450	65.31	58.68	—	61.54	—
	1200	36.62	24.46	—	—	a+b+c
Zr_0La_1	450	—	32.08	—	50.05	—
	900	—	28.35	23.84	51.61	—
	1200	—	57.54	61.75	—	

a: ($La_2Zr_2O_7 = 35{,}17$ nm; b: $La_{0.5}Zr_{0.5}O_{1.75} = 30{,}23$ nm; c: $La_{0.46}Zr_{0.54}O_{1.77} = 31.67$ nm.

Fig. 5. H_2 consumption profiles from H_2—TPR experiments recorded for calcined Zr_1La_0 (*1*), $Zr_{0.85}La_{0.15}$ (*2*), $Zr_{0.7}La_{0.3}$ (*3*), Zr_0La_1 (*4*) samples under air at 450 °C
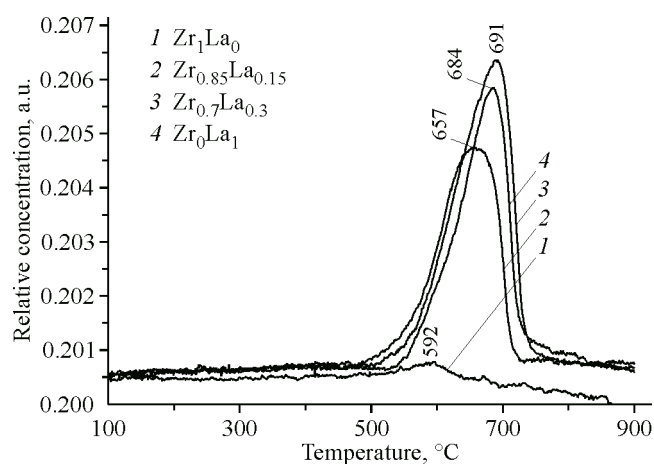
Fig. 6. H_2 consumption profiles from H_2—TPR experiments recorded for calcined Zr_1La_0 (*1*), $Zr_{0.85}La_{0.15}$ (*2*), Zr_0La_1 (*3*) samples under air at 900 °C
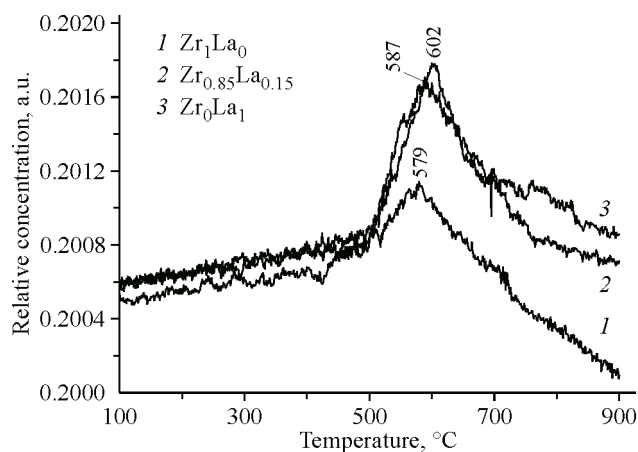
alterations of the nature of interactions between ZrO_2 and La_2O_3. Preliminary experiments on zirconia Zr_1La_0 did not reveal the occurrence of significant reduction processes, as reported also in other publi-

cations [30]. A broad signal appears at a higher temperature, where great H_2 consumption was observed in $Zr_{0.85}La_{0.15}$, $Zr_{0.7}La_{0.3}$, and Zr_0La_1 above 500 °C, corresponding to H_2 uptakes of respectively 1253, 1073, and 437 μmol/g (Table 1). Fig. 5 shows that H_2 consumption profiles recorded for Zr_1La_0, $Zr_{0.85}La_{0.15}$, $Zr_{0.7}La_{0.3}$, and Zr_0La_1 calcined at 450 °C.

As seen, one apparent maximum appears in the temperature range 657—691 °C on the TPR profile corresponding to the reduction of La_2O_3 species. This observation underlines extensive reduction of La_2O_3, which is much more accentuated than that for bare $Zr_{0.85}La_{0.15}$ and $Zr_{0.7}La_{0.3}$.

By contrast, Fig. 6 does not reveal significant H_2 consumption within the error on Zr_1La_0 and Zr_0La_1 calcined at 900 °C ascribed to the reduction of La_2O_3 to LaO_x. The results show a maximum shifting in the temperature range 579—602 °C, which corresponds to H_2 uptakes lower than 100 μmol per gram [22].

It is also worthwhile to note that the H_2 consumption in $Zr_{0.85}La_{0.15}$ slightly exceeds that recorded for Zr_1La_0 and Zr_0La_1 (Table 1). Indeed, a significant lessening in H_2 consumption suggests that ZrO_2 is likely to interact with La_2O_3 [25].

CONCLUSIONS

In this study, the structural and textural modifications of ZrO_2 induced by the La_2O_3 addition, thermal treatment, and reducing process have been investigated. At low temperatures, the lanthanum addition slightly increases the zirconia surface area and do not show any interaction between both oxides. The measured crystallite size of hydroxides remained unchanged for the lanthana samples after calcination at 900 °C, which indicates a good stability of this phase. The specific surface area decreases with an increase in calcination temperatures of the samples, where sintering is very important. On the other hand, surface reconstructions taking place during calcination and the reaction would lead to the formation of surface microstructures ensuring stronger interactions between ZrO_2 and La_2O_3. Therefore, three mixed pyrochlore type oxides are formed and highlighted by XRD and SEM measurements. $TPRH_2$ experiments on zirconia do not reveal the occurrence of significant reduction processes. The changes in the reducibility can reflect some alterations of the nature of interactions between ZrO_2 and La_2O_3. Indeed, a significant lessening in H_2 consumption suggests that ZrO_2 is likely to interact with La_2O_3.

REFERENCES

1. O.V. Karban, O.L. Khasanov, O.M. Kanunnikova. *J. Struct. Chem.*, **2004**, *45*(S1), S147.
2. T. Avalos-Rendon, J. Ortiz-Landeros, G. Fetter et al. *J. Struct. Chem.*, **2011**, *52*(2), 340.
3. S. Boulfrad, E. Djurado. *Solid State Ionic*, **2009**, *180*(14/16), 978.
4. M. Shimazu, K. Yamaji, H. Kishimoto et al. *Solid State Ionic*, **2012**, *224*(14), 6.
5. J. Gao, Z. Hou, X. Liu et al. *Int. J. Hydrogen Energy*, **2009**, *34*(9), 3734.
6. M.A. Soria, C. Mateos-Pedrero, A. Guerrero-Ruiz et al. *Int. J. Hydrogen Energy*, **2011**, *36*(23), 15212.
7. R. Spinicci, P. Marini, S.D. Rossi et al. *J. Mol. Catal. A*, **2001**, *176*(1/2), 253.
8. E.M. Moroz, V.P. Pakharukova, D.A. Zyuzin. *J. Struct. Chem.*, **2013**, *54*(5), 890.
9. V.G. Milt, M.A. Ulla, E.A. Lombardo. *J. Catal.*, **2001**, *200*(2), 241.
10. X. Xu, X. Hu, S. Ren et al. *J. Eur. Ceram. Soc.*, 2016, *36*(7), 1791.
11. D. Bingham, C.A. Leach, B.C.H. Steele. *Mater. Sci. Techn.*, **1987**, *3*(6), 401.
12. E. Kraleva, M.L. Saladino, R. Matassa et al. *J. Struct. Chem.*, **2011**, *52*(2), 330.
13. İ.B. Nilüfer, H. Gökçe, F. Muhaffel et al. *Ceram. Int.*, **2016**, *42*(8), 9443.
14. K.K. Rao, T. Banu, M. Vithal et al. *Mater. Lett.*, **2002**, *54*, 205.
15. A.K. Bhattacharya, A. Hartridge, K.K. Mallick et al. *J. Mater. Sci.*, **1994**, *29*(23), 6076.
16. Y. Matsumure, M. Yoshinaka, K. Hirota et al. *Solid State Commun.*, **1997**, *104*(6), 341.
17. H. Tang, H. Sun, D. Chen et al. *Mater. Lett.*, **2012**, *70*, 48.
18. H. Sun, Y. Ding, J. Duan et al. *Bioresource Techn.*, **2010**, *101*, 953.

19. P. Thangadurai, A. Chandra Bose, S. Ramaray. *J. Mater. Sci.*, **2005**, *40*, 3963.
20. P. Thangaduai, A. Sabarinathan, A. Chandra Bose et al. *J. Phys. Chem. Solids*, **2004**, *65*, 1905.
21. C. Liu, J. Zhang, S. Deng et al. *J. Colloid Interf. Sci.*, **2016**, *474*, 146.
22. M. Ghelamallah, P. Granger. *Fuel*, **2012**, *97*, 269.
23. Y. Li, D. He, Z. Zhu et al. *Appl. Catal. A*, **2007**, *319*, 119.
24. M. Ghelamallah, S. Kacimi, R.I. Fertout. *Mater. Lett.*, **2005**, *59*, 714.
25. M. Ghelamallah, P. Granger. *Appl. Catal. A*, **2014**, *485*, 172.
26. Y. Wu, X. Ni, A. Beaurain et al. *Appl. Catal. B*, **2012**, *125*, 149.
27. U. Martin, H. Boysen, F. Frey. *Acta Crystallogr. Sec.B: Struct. Sci.*, **1993**, *49*, 403.
28. A. Chatterjee, S.K. Pradhan, A. Datta et al. *Mater. Res.*, **1994**, *9*, 263.
29. Salah-ud Din, A. Kaleem. *Mater. Chem. Phys.*, **1998**, *53*(1), 48.
30. K. Otsuka, Y. Wang, M. Nakamura, *Appl. Catal. A*, **1999**, *183*(2), 317.